PHILOSOPHICAL TRANSACTIONS A

royalsocietypublishing.org/journal/rsta

Research

Article submitted to journal

Subject Areas:
computational ice accretion modeling, glaze icing phenomena, immersed boundary methods, rough wall heat transfer, thin water film dynamics, turbulent heat transfer in icing

Keywords:
aircraft icing, CFD, glaze ice accretion, immersed boundary method, water film dynamics, rough thermal wall function, ice accretion simulation

Author for correspondence:
Guilherme Araujo da Silva
e-mail: gasilva@aerothermal.co

THE ROYAL SOCIETY PUBLISHING

Advancing the iceAccretionFoam Solver: Glaze Ice Accretion

Rafael M. H. Carvalho[1], Jayme R. Teixeira da Silva[1], Pedro C. de Souza Villela[1], Caio F. Rafael[2], Guilherme A. Lima da Silva[2] and Hrvoje Jasak[3,4]

[1]Av. Pompéia, 634 cj 107, Sao Paulo, SP, Brazil
[2]201 Biscayne Blvd., Suite 1200, Miami, FL, USA
[3]Cambridge University, Cambridge, UK
[4]459 Southbank House, London, UK

This paper presents a three-dimensional ice accretion tool for rime and glaze ice types, developed based on foam-extend 5.0, in a new solver for icing applications: iceAccretionFoam. The purpose of this paper is to analyze the hydrodynamics of water films using the finite area method, rough turbulent heat transfer modeling, the immersed boundary method to change the geometry, flow-ice shape interaction, impingement by Eulerian formulation, and external flow solutions with the compressible solver rhoPimpleFoam. The work develops and implements a unified computational fluid dynamics (CFD) tool that is capable of modeling the entire process in one 3D solver. The present work describes the second part of the initial development of a CFD tool, focusing on the water film hydrodynamic modeling, turbulent rough heat transfer, compressible flow unsteady solver, and ice growth with a model based on liquid water film height time derivative that is applied for both rime and glaze types. The implementation was accurate and yielded acceptable initial results, as indicated by preliminary verification carried out by the authors.

1. Introduction

Historically, CFD has played a role in icing simulations, but fully integrated CFD solutions are not yet available. Since the early years of icing simulations, developers have primarily used the three-dimensional (3D) potential or Euler CFD to calculate the pressure coefficient, model Lagrangian impingement on exposed surfaces, and predict glaze and rime ice shapes with the support of boundary layer calculations by integral procedures.

The glaze ice simulation requires a thermal boundary layer, which at minimum follows the Reynolds analogy between momentum and heat transfer. In addition, it involves applying the first law of thermodynamics to the water flowing on the surface after impingement. This process results in "wet" ice growth, characterized by the presence of a water film that freezes when the solidification enthalpy and droplet kinetic heating are transferred through convective heat transfer. These thermal effects were traditionally modeled using simplified models outside the CFD tool, relying on classical icing mathematical models.

The present work proposes a unified CFD tool capable of modeling the entire process with a 3D spatial and temporal resolution, using the existing foam-extend 5.0 numerical libraries in a new solver for icing applications: iceAccretionFoam. This includes hydrodynamics of water films in a finite-area formulation, mesh interpolation after ice growth using an immersed boundary approach, a compressible flow solver based on rhoPimpleFoam, impingement via an Eulerian formulation based on driftEulerFoam, and rough turbulent heat transfer wall functions for α_t and μ_t as developed by Silva et al. (1) with the modified correlation for St_k(2). According to Stefanini (3; 4), it is necessary to model the laminar-turbulent transition properly to get the size, angle, and position of the glaze horns; however, it will not be implemented in this work due to the scope of the initial development.

Some of these solutions are presented in this paper, while others will be developed in future stages, such as water hydrodynamics regimes, laminar-turbulent transition, SLD effects, and thermal ice protection systems. It is imperative to have a 3D code that works for icing to properly simulate antennas, probes, radars, swept wings, propellers, engine inlets, advanced air mobility aircraft, and drones - not just simple 2D airfoils extruded into 3D by making cuts normal to the leading-edge line.

In terms of 3D icing codes, NASA LEWICE3D (5) is a pioneering tool for addressing 3D icing. This code uses flow solutions from external CFD and calculates droplet trajectories with the Lagrangian formulation. Although the external flow is solved in 3D, the ice growth is modeled in 2D, resulting in a quasi-3D solution to the ice-accretion problem. Instead of following the shear lines or solving them in 3D, the code makes several cuts perpendicular to the leading-edge line of the wing. Depending on the degree of sweep, the shear lines make an accentuated curve after stagnation and deviate significantly from the normal-direction cuts made by LEWICE3D (5). The simplifications inherent in a quasi-3D approach, such as assumptions about runback water hydrodynamics and flow direction, introduce errors that reduce the code's ability to accurately predict glaze ice shapes, particularly on swept wings and other complex 3D features.

The FENSAP (6) code, initially developed by the team of Prof. Habashi at McGill University, uses a 3D flow solution from CFD but calculates the droplet trajectories using an Eulerian formulation. In this method, the observer does not travel in the droplets but is fixed in a control volume. The solution adds three equations for droplet transport in Reynolds conservation form: momentum, energy, and mass. In addition to the impingement module, the FENSAP code also includes modules for heat transfer and ice growth. The three modules plus CFD are solved interactively to calculate the final ice shape. As the ice grows, the geometry changes with each iteration, influencing the flow and impingement, which in turn affects heat transfer and, consequently, ice growth in a coupled manner. The water runback is represented as a continuous film until it either evaporates or freezes. Runback is a critical factor in the accretion of glaze ice but is absent in rime ice, where the water freezes instantly upon impact. Thus, glaze ice formation requires applying the first law of thermodynamics to the water runback flow, whereas rime ice does not. FENSAP applies conservation of mass, energy, and momentum to solve the water film. However, it does not account for other runback water flow regimes, such as beads and rivulets, which depend on superficial tension along the runback flow.

Another important fact is that four codes are involved: CFD, droplets, heat transfer, and ice growth. This integration can lead to information loss when transferring data between codes. In addition, the assumptions made by one code may be more restrictive or simplified than those of others, including the 3D CFD solution, limiting the accuracy of the predictions. Finally, it remains unclear whether the code performs fully 3D calculations or adopts a quasi-3D approach using 2D normal slices, as in LEWICE3D.

Regarding acceptance by authorities, no 3D code is widely accepted, despite 2D codes being recognized and accepted for specific applications, mainly on wings. This weak acceptance is due to the fact that the

technology for 3D ice accretion has not yet been entirely developed. For example, no existing code can accurately reproduce the formation of ice lobster tails on swept wings. Another important factor is the set of assumptions for each code that may limit its general application in 3D. Therefore, the advancement of 3D ice simulation depends on improving or eliminating simplifying assumptions.

(a) OpenFoam applied to Aircraft Glaze Icing

Beld (7) distinguishes between two types of ice accretion on aircraft surfaces: rime ice and glaze ice. Rime ice forms at temperatures well below freezing, freezing almost entirely upon impact and minimally altering the aircraft's shape. Glaze ice, on the other hand, forms at temperatures just below 0 °C, with partially frozen impinging droplets creating a liquid film that runs back, freezes downstream, and can significantly alter aerodynamic shapes. The work illustrates these ice accretions, but does not provide a thorough validation.

Another work is from Li and Paoli (8), whose thermodynamic model is based on the Messinger model, which has been used in several commercial icing codes. Different icing conditions result in different types of ice accretion: rime ice forms when supercooled water droplets freeze instantaneously upon impact on the aircraft wings, while glaze ice occurs when the environmental temperature is not low enough, allowing the droplets to run back as liquid water before freezing. The paper does not provide detailed information on the validation of the glaze ice shape results.

(b) Objective

The objective of this paper is to present a 3D ice accretion tool for rime and glaze ice types, developed based on foam-extend 5.0. In addition to being fully 3D, the tool has several key characteristics:

- Compressible Unsteady Reynolds-Averaged Navier-Stokes (URANS) solver based on rhoPimpleFoam, which combines SIMPLE and PISO numerical schemes for compressible flow.
- Droplet trajectories and impingement solver based on incompressible driftEulerFoam.
- Calculation of runback water flows with movement driven by shear forces, pressure gradient, and parallel momentum of impinging droplets. This is implemented with the support of a water hydrodynamics model that solves the conservation of mass, momentum, and energy in a thin water film. This model is used to obtain an evaluation of the "wet" growth, which is the freezing of liquid water on the surface after impingement. This is implemented using the finite area method (FAM) of Tukovic and Jasak (9).
- Rough turbulent heat transfer coefficient determined by a wall function specially developed by Silva et al. (1) for heat diffusion. This is based on an innovative correlation proposed by Stefanini et al. (2) and recently mentioned by Lima da Silva (10).
- Immersed Boundary Method (IBM) (11), which updates the boundary of the solid surface and interpolates the mesh around the new surface created by ice growth.
- Capability to incorporate either a user-defined droplet distribution or a Langmuir D-type distribution with several bins based on the mean volumetric diameter (MVD).

(c) Scope

The present paper is focused on an implementation of the rime and glaze accretion simulation with runback water film on the surface, turbulent rough heat transfer, compressible flow unsteady solver, Eulerian phase transport solution, and ice growth with the same background mesh.

It is important to note that only one CFD code performs all calculations and no external tool is used. This allows for the model improvement and the elimination of assumptions required by the case, achieved by directly modifying the in-house source code. The rime and glaze ice are calculated by the same set of equations in one code.

(d) Structure of the Work

It is important to present the unique features of the developed icing tool, as well as the mathematical models used and its computational implementation. A test case is defined and preliminary verification is carried out. As this work is not final because the development will require more physical phenomena to be represented, for instance, a laminar-turbulent transition triggered by roughness or a complete water hydrodynamics with rivulets, beads, and film regimes, the results of this paper only need to verify the basic physics as a sanity check and show an acceptable trend.

2. Mathematical Models

(a) External Continuous Flow

The equations for the main or continuous flow of air in the present work are provided below, although not in the sequence in which they are solved within the compressible PIMPLE loop implementation in rhoPimpleFoam.

The pressure equation for the main continuous flow is solved by employing the decoupled equation p. The use of the decoupled method is justified because icing scenarios operate in the compressibility limit region, which is far from the transonic or sonic regimes.

$$\frac{\partial}{\partial t}(\psi\, p) + \nabla \cdot \phi - \nabla \cdot (\rho\, r_{UA}\, \nabla p) = 0 \tag{2.1}$$

Once the pressure solution is determined, the velocities of the flow field, represented by U, are subsequently updated by:

$$\mathbf{U} = \mathbf{U} - r_{UA}\, \nabla p \tag{2.2}$$

Therefore, the equation for momentum conservation can be completely resolved:

$$\frac{\partial}{\partial t}(\rho\, \mathbf{U}) + \nabla \cdot (\rho\, \mathbf{U} \otimes \mathbf{U}) + \nabla \cdot \boldsymbol{\tau} = -\nabla p \tag{2.3}$$

Following the update of p and U, the momentum solution allows the energy conservation problem to be solved using the enthalpy equation.

$$\frac{\partial}{\partial t}(\rho\, h) + \nabla \cdot (\rho\, h\, \mathbf{U}) - \nabla \cdot (\alpha_{\text{eff}}\, \nabla h) = \frac{Dp}{Dt} + \Phi \tag{2.4}$$

The term representing viscous dissipation becomes increasingly significant for flows with Mach numbers approaching 0.3 and is defined in Eq. (2.4) as follows:

$$\Phi = \boldsymbol{\tau} : \nabla \mathbf{U} \tag{2.5}$$

In Eq. (2.4), the term related to pressure work illustrates the compression and expansion of the airflow:

$$\frac{Dp}{Dt} = \frac{\partial p}{\partial t} + \mathbf{U} \cdot \nabla p \tag{2.6}$$

In the equations, some important variables are defined as follows:

- r_{UA}: The reciprocal of the diagonal coefficient of the discretized momentum equation, given by $r_{UA} = \frac{1}{A}$, where A represents the accumulated implicit terms.
- ψ: The compressibility coefficient, defined as $\psi = \left(\frac{\partial \rho}{\partial p}\right)_T$.
- ϕ: The mass flux across the faces of the control volumes, defined as $\phi = \rho\, \mathbf{U} \cdot \mathbf{S}_f$, where $\mathbf{S}_f$ is the face area vector.
- Φ: only accounts for the dissipation heat term but neglects the effects of the bulk viscosity because the regime in ice operation is far from the transonic or sonic regimes.

- $\alpha_{\text{eff}} = \alpha_t + \alpha_l$, where α_{eff} is called effective thermal diffusivity that joins thermal turbulent diffusivity with molecular or laminar diffusivity, which is $\alpha_l = \left(\frac{k}{\rho \cdot c_p}\right)_{\text{ideal gas}}$.

(b) External Eulerian Phases Flow

The incompressible dispersed phase, according to the driftEulerFoam solver, defined by $U_{phase,i}$ and α, is calculated considering the following definitions. To estimate the air drag on the droplet, driftEulerFoam applies the Schiller-Naumann correlation (12).

$$\left\|\vec{U}_{rel}\right\| = \left\|\vec{U}_{phase,i} - \vec{U}\right\| \tag{2.7}$$

$$Re_{rel} = max(\,2.4,\, \left\|\vec{U}_{rel}\right\| \cdot \frac{d}{\nu_D}) \tag{2.8}$$

$$C_d = max\left[\,0.5, \frac{24}{Re_{rel}}(1 + 0.15 \cdot Re_{rel}^{0.687})\right] \tag{2.9}$$

$$DragPf = \frac{3}{4} \cdot Cd \cdot \frac{\rho_C}{\rho_D} \cdot \frac{\left\|\vec{U}_{rel}\right\|}{d} \tag{2.10}$$

The equation for $U_{phase,i}$, droplet phase velocity, is defined as follows:

$$\begin{aligned} \frac{\partial\, \tilde{\mathbf{U}}_{\mathbf{phase,i}}}{\partial t} + \nabla \cdot (\vec{\boldsymbol{\phi}}_{\boldsymbol{cont}} \cdot \tilde{\mathbf{U}}_{\mathbf{phase,i}}) = \\ \mathbf{g} + DragPf(\tilde{\mathbf{U}}_{\mathbf{rel}}) - \frac{3}{4} C_d \cdot \left\|\vec{U}_{rel}\right\| \cdot \nu_t \cdot \frac{\nabla \alpha_{\mathbf{phase,i}}}{d} \end{aligned} \tag{2.11}$$

Here, ϕ_{cont} is the incompressible flux of the continuous phase or the main flow. It is related to compressible flux ϕ and gas density ρ by the relation:

$$\rho \cdot \phi_{cont} = \phi \tag{2.12}$$

Here, ϕ_{cont} is the volume per time and ϕ is the mass per time used in the main flow solution. The equation for $\alpha_{\mathbf{phase,i}}$, volumetric fraction, is listed below:

$$\frac{\partial \alpha_{\mathbf{phase,i}}}{\partial t} + \nabla \cdot (\tilde{\phi}_{\mathbf{phase,i}} \cdot \alpha_{\mathbf{phase,i}}) = 0 \tag{2.13}$$

Here, $\phi_{phase,i}$ is the flux of the droplet phase or the flow of the dispersed phase. The $DragPf$ is the drag prefactor term, which is part of the sphere drag calculation. Here, i represents one diameter in the droplet distribution of n bins.

(c) Runback Water Flow

The second significant feature of ice accretion simulations is the possible presence of a liquid wall surface film undergoing a phase change: solidification or melting. A consequence of this wall-film physics is that the surface freezing caused by the impact of the droplets may occur at locations other than the impact point itself, which is determined by the interaction between melting/solidification and wall-film transport to the environment. This process is modeled using the finite-area method approach on the deforming surface.

(i) Mass Conservation

The freezing fraction ff, representing the amount of water frozen in the control volume, can have an assumed value when solving the mass conservation equation; each time it is updated with the value of the function below. Therefore, the calculation of temperature ff is one step behind. This approach means that ff is considered constant when solving the mass conservation equation. Since ff is constant, the

solidification rate is zero. This means that the rate of change of M_{solid} is zero and the rate of change of M_{liquid} is influenced only by the other processes.

Using the relationships:

$$\begin{aligned} \frac{\partial m}{\partial t}_{ice,cv} &= ff \cdot \frac{\partial m}{\partial t}_{total,cv} = ff^* \cdot \frac{\partial m}{\partial t}_{liquid,cv} \\ \frac{\partial m}{\partial t}_{total,cv} &= \frac{\partial m}{\partial t}_{liquid,cv} + \frac{\partial m}{\partial t}_{ice,cv} \\ \Rightarrow ff^* &= \frac{ff}{1-ff} \end{aligned} \tag{2.14}$$

The differential equation for the conservation of the mass of liquid water in the control volume (indicated as cv), considering the divergence representation for mass flow in and out, can be written as:

$$\frac{\partial m}{\partial t}_{liquid,cv} = \dot{m}_{in} - \dot{m}_{out} + \dot{m}_{imp} - \dot{m}_{evap} - \frac{\partial m}{\partial t}_{ice,cv} \tag{2.15}$$

In the differential form for the conservation of the mass for the finite-area water film, Eq. (2.15) becomes:

$$\begin{aligned} \frac{\partial h_f}{\partial t} + \nabla \cdot (\phi_s \cdot h_f) &= 2 \cdot S_m - S_f - S_e \\ S_m &= \frac{\sum \alpha_i \cdot \phi_{phase,i}}{|A|} \\ S_f &= ff^* \cdot \frac{\partial h_f}{\partial t}_{cv} \\ S_e &= \frac{\dot{m}^{"}_{evap}}{\rho_w} \end{aligned} \tag{2.16}$$

Where ϕ_s and h_f are the flux of runback water and h_f is the height of the film. In addition, variables S_m, S_f, and S_e are source terms on the right-hand side due to impingement, freezing, and evaporation, respectively. This equation represents the conservation of the mass of liquid water in the control volume, taking into account the freezing processes that occur in the control volume, under the assumption that the fraction of solidified mass ff^* remains constant during the ice growth step.

(ii) Momentum Conservation

The momentum conservation principle is applied to the water on the surface to get the following equation:

$$\begin{aligned} \rho_w \frac{\partial (V\vec{v})}{\partial t} + \nabla \cdot (\phi_w \vec{v}) &= \tau_w + V \nabla p_L + S_v \\ p_L &= p_{bl} + p_d + p_\sigma + p_h \\ p_{d,i} &= \frac{\rho \left(\mathbf{v}_{d,i}\right)_n^2}{2} \\ p_\sigma &= -\sigma \nabla_s \cdot \left(\nabla_s h_f\right) \\ p_h &= -\rho_L \mathbf{n} \cdot \mathbf{g} h_f \\ \overline{\mathbf{S}}_v &= \frac{\sum_i m_{d,i} \left(\mathbf{v}_{d,i}\right)_t}{\mathrm{d}t} \end{aligned} \tag{2.17}$$

Where $\overline{\mathbf{S}}_v$ is a source term, p_h is the effect of gravity, p_σ is the surface tension, p_d is the pressure of the impinging droplets and p_{bl} is the main flow pressure at the edge of the boundary layer. The differential equation for momentum conservation for the finite area, excluding the effects of surface tension, accounting for the film height, is expressed as follows:

$$\frac{\partial h_f \vec{U_s}}{\partial t} + \nabla \cdot (\phi_{2s} \cdot \vec{U_s}) + 0.0125 \cdot C_{f,w} \left|\vec{U_s}\right| \cdot \vec{U_s} = (S_\tau + S_i + S_g) \cdot \vec{b}_{\|} + S_{gradP} + S_{bl}$$

$$\begin{aligned}
\phi_{2s} &= \phi_s \cdot h_f \\
S_\tau &= \frac{\vec{\tau} \cdot h_f}{\rho_w} \\
S_i &= \frac{\sum \alpha_i \cdot \phi_{phase,i} \cdot \vec{U}_{phase,i}}{|A|} \\
S_g &= \vec{g} \cdot h_f \\
S_{graP} &= -\vec{\nabla}(p_s \cdot h_f) \\
S_{bl} &= \frac{p_s}{\rho_w} \cdot \vec{\nabla} h_f
\end{aligned} \tag{2.18}$$

The source terms S_τ represent the shear of the external flow on the surface of the water film, S_i is the parallel momentum of the impinging droplets, S_g is the effect of gravity, S_{graP} is the effect of the pressure gradient of the external flow, S_{bl} is the pressure effect of the boundary layer on the height of the film, $C_{f,w}$ is the viscous drag coefficient between the film and the solid surface.

(iii) Energy Conservation

The First Law of Thermodynamics applied to liquid water can be written as follows.

$$\frac{dU}{dt} + \nabla \cdot (\vec{v}H) - k \cdot \nabla^2 T = \dot{H}_{imp} - \dot{H}_{evap} + \dot{H}_{freeze} - \dot{q}_{conv} + \dot{q}_{\text{wall}} \tag{2.19}$$

The terms $\dot{H}_{imp}$, $\dot{H}_{evap}$, $\dot{H}_{freeze}$, $\dot{q}_{conv}$, and $\dot{q}_{wall}$ are the enthalpy change rates and heat transfer rates. The temperature of the water in Kelvin is represented by T_f. The rate of change in enthalpy due to the impingement of water droplets denoted as $\dot{H}_{\text{imp}}$, while $\dot{H}_{\text{evap}}$ represents the rate of change in enthalpy due to evaporation. The symbol $\dot{H}_{\text{freeze}}$ represents the rate of change in enthalpy due to freezing. The heat flux rate due to convection and the heat flux rate between the wall and water are represented by $\dot{q}_{\text{conv}}$ and $\dot{q}_{\text{wall}}$, respectively. The density of the foam-ext water is denoted as ρ, and the specific heat capacity of the foam-ext water is represented by c. The velocity field of the water flow is given by $\vec{v}$. Lastly, V denotes the volume of the control volume.

$$\frac{\partial h_f \cdot T_f}{\partial t} + \nabla(\rho_w \cdot C_w \cdot \phi_{2s} \cdot T_f) - k \cdot h_f \cdot \nabla^2 T = h_{conv} \cdot (T_\infty - T_f) + S_{mi} + S_{Hf} + S_{He}$$

$$\begin{aligned}
S_{mi} &= \rho_w \cdot C_w \cdot S_m \cdot T_d \\
S_{Hf} &= ff^* \cdot \frac{\partial h_f}{\partial t} \cdot \rho_w \cdot h_{ls} \\
S_{He} &= (1 - ff^*) \cdot \overset{"}{m}_{evap} \cdot h_{lv}
\end{aligned} \tag{2.20}$$

The source terms of Eq. (2.20) are listed herein: S_{mi} is the enthalpy of stagnation of the impinging droplets on the surface, S_{Hf} is the enthalpy of freezing water parcel, and S_{He} represents the enthalpy of evaporation of the remained liquid water. In addition, some definitions are required to define the energy conservation of Eq. (2.20) properly.

$$T_d = T_\infty + \frac{V_d^2}{2 * C_w} \tag{2.21}$$

$$\dot{q}^{"}_{wall} = \alpha_{\text{eff}} \cdot \nabla h = \alpha_{\text{eff}} \cdot c_p \cdot \nabla T \tag{2.22}$$

$$h_{conv} = \left| \frac{\dot{q}^{"}_{wall}}{T_{wall} - T_\infty} \right| \tag{2.23}$$

Where T_d is the stagnation temperature of the droplets, $\dot{q}^{"}$ is the convective heat flux in the wall and h_{conv} is the coefficient of convective heat transfer. As per Spalding (13), the water evaporation mass flux by convective mass transfer is calculated by:

$$\dot{m}''_{evap} = g_m \cdot \mathrm{B}_m \tag{2.24}$$

$$g_m = \frac{h_{conv}}{c_p} \cdot \mathrm{Le}^{2/3} \cdot \frac{\ln\left(1 + \mathrm{B}_m\right)}{\mathrm{B}_m} \tag{2.25}$$

where Le is the Lewis number, used to establish the analogy between heat and mass transfer, g_m is the potential or convective mass coefficient, the last term in the right side, $(\ln(1 + \mathrm{B}_m))/\mathrm{B}_m$, is the blowing enthalpy factor, caused by evaporation, in the thermal boundary layer, c_p is the specific heat, and B_m is the convective mass transfer driven force calculated by the following expression (13; 14):

$$\mathrm{B}_m = \frac{mf_{H2O,S} - mf_{H2O,G}}{mf_{H2O,S} - 1} \tag{2.26}$$

where mf represents the mass fractions at the surface of the film S at film temperature and in the gas flow G at freestream temperature by considering saturated conditions.

(d) Ice Growth Model

In contrast to the previous code of Teixeira da Silva et al. (15; 16) for rime ice accretion in foam-ext, which was the preliminary development of the present paper, the ice size is not related to impingement alone, but to the rate of change in mass in the liquid film, which comes from the derivative in time of the liquid h_f in the control volume, solved through the conservation of the mass of the water film in Eq. (2.16).

$$h_{ice} = ff^* \cdot \left(\frac{dh_f}{dt}\right)_{cv,liquid} \cdot \frac{\rho_{liquid}}{\rho_{ice}} \cdot \Delta t_{ice} \tag{2.27}$$

where Δt_{ice} is the time of ice accretion in the multistep solver. In this paper, it is set to 30 s of ice growth for each 0.1 s of the flow solution. This is a way to accelerate the solution. The densities ratio $\frac{\rho_{liquid}}{\rho_{ice}}$ is the same as the validated implementation for rime ice accretion in the previous work (15) of the Lewice 2D code (17). The present work uses the constant T_∞ as the basis for the calculation of the ice density, instead of the variable recovery temperature T_{rec} along the surface of the airfoil. The variable in the field h_{ice} is used to deform the covered boundary surface.

(e) Freezing Fraction

The current work utilizes the concept of freezing fractions to model the freezing process. Unlike conventional modeling, which considers the total mass of water, this approach defines a freezing fraction specifically for partial solidification of the liquid control volume while maintaining a constant solidification temperature of 273.15 K. This ensures an accurate representation of the freezing behavior of the liquid. Equation (2.14) shows the relation between the freezing fraction ff of the overall water mass and the ff^* of the liquid mass, since the ice mass is not included in the model of the liquid water film.

In this work, for simplicity, an algebraic approach was adopted for the freezing fraction as defined by Crank (18). It also employs the method of assumed states (MOAS) from Raw and Schneider (19) for the enthalpy method, where the phase is assumed, and then the energy equation is solved iteratively. Thus, the freezing fraction is defined as follows.

$$T_{diff} = \frac{T_f - 273.15}{273.15} \tag{2.28}$$

$$ff = 1 - \left(0.5 + 0.5 \tanh\left(K_{Freezing} \cdot T_{diff}\right)\right) \tag{2.29}$$

The constant $K_{Freezing}$, although arbitrarily chosen, is typically set at a large value to minimize the partial freezing zone, as depicted in Figure 1, thereby making the model closely resemble reality, which features an abrupt transition. In this work, a value of $273.15 \cdot 10^8$ was adopted. As tracking the transient movement of the freezing front is not required in this paper, and there is no need for ice or mushy region properties, only the liquid water is considered in the model.

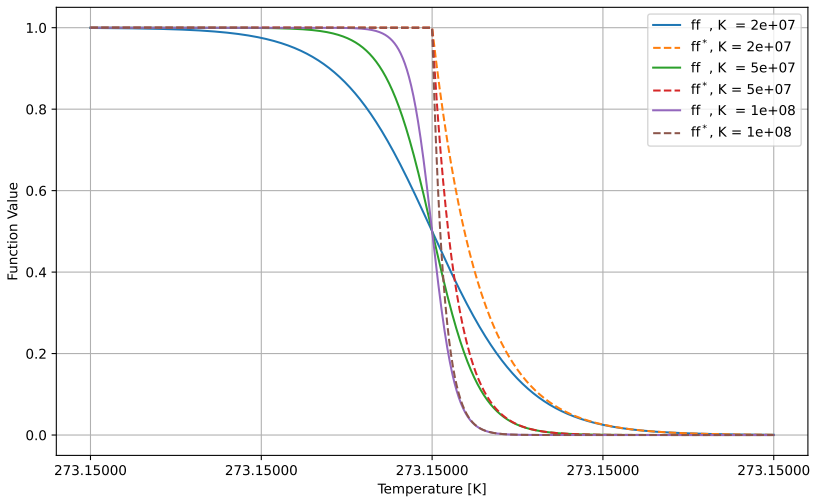

Figure 1: Freezing fraction definition around 273.15 K, where $K = K_{Freezing}/273.15$

(f) Wall Boundaries Momentum and Heat Transfer

This study applies an adapted form of the wall functions as implemented in OpenFOAM ext. 1.6 by Lima da Silva et al. (1) and reported by Lima da Silva et al. (10), focusing on momentum and thermal diffusivity, μ_t and α_t, near the wall. The model for momentum transfer leverages Tapia's approach (20) with modifications similar to those explored in icing studies. Convective heat transfer plays a crucial role as it acts primarily as the heat sink in the energy equation for the water film on the surface. This process determines the region where the ice forms after the liquid film impacts and flows near its solidification temperature. The driving force behind the motion of the water film predominantly comes from the wall shear forces, with additional contributions from pressure gradients and the parallel momentum of impacting droplets.

(i) Fully Turbulent Momentum Transfer over Rough Surfaces

The research conducted by the Stanford University team between 1958 and 1983 on aspects such as momentum and thermal boundary layers related to skin friction, heat transfer, and the turbulent Prandtl number (Pr_t) (14; 21; 22) continues to serve as a fundamental reference for icing research activities by organizations such as NASA (23), ONERA (24), and Makkonen (25). These studies used equivalent sand

grain heights to categorize flow regimes over rough surfaces.

$$\text{Flow regimes over rough surfaces} \begin{cases} Ks^+ \leq 5 & \text{smooth} \\ 5 < Ks^+ < 70 & \text{transitionally rough} \\ Ks^+ \geq 70 & \text{fully rough} \end{cases} \tag{2.30}$$

The Reynolds number calculated for the height of the roughness in the wall coordinates $Ks^+ = u_\tau Ks/\nu$, serves as a measure to assess the hydraulic smoothness of a surface. When Ks^+ is below 5, the surface qualifies as smooth. Conversely, if Ks^+ exceeds 70, the viscous sublayer vanishes, and the skin friction on the wall becomes independent of the Reynolds number. Under these conditions, pressure drag, which results from dynamic pressure impacting the rough surface upstream, becomes the dominant factor. However, drag continues to influence flow, affecting heat transfer and changing with an increase in Re (26).

The velocity profile in wall coordinates $u^+ = u/u_\tau$ and $y^+ = yu_\tau/\nu$ is given by:

$$u^+ = \frac{1}{\kappa} \ln\left(\frac{32.6 \cdot y^+}{Ks^+} + 1\right) \approx \frac{1}{\kappa} \ln\left(\frac{32.6 \cdot y^+}{Ks^+}\right) \tag{2.31}$$

where $u^+ = u/u_\tau$, $\kappa = 0.41$ is a constant, u is the mean velocity at point p, $u_\tau = \sqrt{\tau/\rho}$ is the shear velocity, and τ is the shear stress.

The velocity of the flow near the rough wall is shown here:

$$u^+ = \frac{1}{\kappa} \ln\left(E \cdot y^+\right) - \Delta B \tag{2.32}$$

In this context, $E = 9.8$ and $\kappa = 0.41$ are constants. Nonetheless, the code adheres to the Cebeci model (27) in order to compute ΔB using Eq. (2.32):

$$\Delta B = \begin{cases} 0 & Ks^+ \leq 2.5 \\ \frac{1}{\kappa} \ln\left[\frac{K_s^+ - 2.25}{87.75} + C_s K_s^+\right] \sin[0.4258 \cdot (\ln K_s^+ - 0.811)] & 2.5 < Ks^+ < 90 \\ \frac{1}{\kappa} \ln\left(1 + C_s K_s^+\right) & Ks^+ \geq 90 \end{cases} \tag{2.33}$$

Where C_s depends on the shape and distribution of the roughness elements and,

$$y^+ = y\frac{\rho C_\mu^{0.25} k^{0.5}}{\mu} \qquad and \qquad K_s^+ = K_s\frac{\rho C_\mu^{0.25} k^{0.5}}{\mu} \tag{2.34}$$

Equation (2.34) is applicable when the turbulent kinetic energy is more than 20, and C_μ is a constant with a value of 0.09. The turbulent viscosity is then calculated using the foam-ext wall function known as *mutRoughWallFunction*:

$$\mu_t = \mu\left(\frac{y^+\kappa}{\ln\left(Ey^+/e^{\kappa\Delta B}\right)} - 1\right) \tag{2.35}$$

(ii) Momentum wall function for rough surfaces

Equating Eq. (2.31) to Eq. (2.32) reveals the relationship between the constant C_s and the Stanford model applied to rough surfaces experiencing turbulent flow:

$$C_s = \frac{E}{32.6} - \frac{1}{K_s^+} \tag{2.36}$$

For the application of the Stanford model in conventional icing codes via the momentum wall function, Eq. (2.36) is essential. It ensures that icing engineers can retain consistent K_s values in their simulations. As K_s^+ approaches an infinite value, with $E = 0.98$, the C_s from Eq. (2.36) stabilizes at roughly 0.3, characterizing a fully rough surface. Consequently, within the proposed model, Eq. (2.33) becomes obsolete,

and the function ΔB is expressed as:

$$\Delta B = \frac{1}{\kappa} \ln\left(1 + C_s K_s^+\right) \tag{2.37}$$

Substituting Equation (2.37) into Eqs. (2.32) and (2.35) results in the determination of u^+ and μ_t, respectively. Comparisons were made between the ranges of the rough flow regime based on K_s^+ and those of the Stanford model, as defined in Eq. (2.30). Consequently, all equations remain unchanged except for replacing ΔB in Eq. (2.33) with (2.37), and introducing the variable function C_s in Eq. (2.36) in place of the constant C_s specified by the user. Notably, this paper focuses on adjusting the momentum wall functions only to align with standard models used in the ice-accretion sector without significant modifications. The scope of the paper specifically excludes regions of separated flow, adverse pressure gradients, compressible flows, and accelerated flows. These limitations are inherent in foam-ext's momentum wall function model.

(iii) Fully Turbulent Heat Transfer Over Rough Surfaces

The analogy between momentum and heat transfer is relevant for turbulent flow, although it does not apply to the rough sublayer, which is located physically under the main boundary layer flow, and can be stated as follows:

$$\alpha_t = \frac{\mu_t}{Pr_t} \tag{2.38}$$

The derived expression takes into account the turbulent viscosity μ_t, the thermal diffusivity α_t, and the turbulent Prandtl number Pr_t. Equations (2.31) and (2.38), together with the definitions of t^+ and the assumption of a consistent Pr_t throughout the entire turbulent boundary layer, contribute to the resulting expression.

$$t^+ = \delta t_0^+ + \frac{Pr_t}{\kappa} \ln\left(\frac{32.6 \cdot y^+}{Ks^+}\right) \tag{2.39}$$

The initial term on the right-hand side of Eq. (2.39) pertains to the thermal resistance within the viscous sublayer, which is influenced by the surface roughness. Because this sublayer is sequentially aligned with the fully turbulent layer, roughness decreases the effectiveness of heat transfer, acting as thermal resistance in series, thus decreasing the enhancement effect (26). As a result, the alteration in the t^+ profile is represented by a roughness St.

$$\delta t_0^+ = \frac{1}{St_k} = \frac{\rho c_p u_\tau}{h_k} \tag{2.40}$$

Thus, a thermal convection correlation in the sublayer can be defined in a useful form:

$$St_k = C \cdot (Ks^+)^a \cdot Pr^b \tag{2.41}$$

The heat and momentum analogy was formulated in terms of the molecular Prandtl number Pr, as well as the experimental calibration constants C, a, and b. Kays and Crawford (14) developed this analogy in terms of Pr_t, Pr, and C_f.

$$St = \frac{C_f/2}{Pr_t + \dfrac{\sqrt{C_f/2}}{St_k}} \tag{2.42}$$

The heat and momentum analogy of turbulent thermal boundary layers is addressed using rough skin friction, C_f, in the denominator of Eq. (2.42). The initial term denotes this analogy, while the second term indicates the distinct impact of roughness on the viscous sublayer of the thermal boundary layer. Consequently, as seen in Eqs. (2.40) and (2.42), the analogy factor Pr_t decreases due to the thermal resistance of the sublayer, which is influenced by the correlation between $\sqrt{C_f/2}$ and St_k. With lower values of St_k and higher values of C_f, the analogy diverges more significantly from Pr_t.

The *alphatWallFunction* code presumes that Eq. (2.38), which describes the correlation between heat and momentum transfer, remains throughout the layer. Users can specify a constant Pr_t, making Eq. (2.38) the only method available for simulating heat transfer. This is because there is no thermal wall function

available for uneven surfaces that encompass both a fully turbulent region and the region of the boundary layer influenced by roughness.

(iv) Thermal Wall Function For Rough Surfaces

This paper suggests adopting the Stanford model within the momentum wall function, as is commonly applied in icing simulations. Furthermore, it introduces an innovative model for the thermal wall function, which remains unexplored in the icing area. This approach aims to improve the accuracy of momentum and heat transfer predictions on rough surfaces. The conventional equation (2.38) neglects the impact of the thermal resistance of the viscous sublayer, focusing solely on the fully turbulent thermal resistance. Consequently, the analogy Pr_t must be adjusted by a factor influenced by the properties of the fluid and the roughness of the sublayer, K_s, $\sqrt{Cf/2}$, Pr_t and Pr, which resemble the structure of equation (2.42).

The present authors suggest that one employs the momentum and heat transfer analogy factor to represent flow on rough surfaces.

$$\eta = \frac{1}{Pr_t + \frac{\sqrt{C_f/2}}{St_k}} \tag{2.43}$$

The calculation of St_k is described in Eq. (2.41), incorporating the constants $a = -0.45$, $b = -0.8$ and $C = 1.42$, as suggested by Stefanini et al. (2) and Lima da Silva et al. (10). Makkonen (25) evaluated this in relation to the roughness characteristic of a densely packed pyramidal surface with foam extension. The foam-ext solver employs the following equations to compute C_f.

$$\frac{u_\tau}{u} = \sqrt{C_f/2} \quad \text{and} \quad u_\tau = \sqrt{\tau/\rho} \quad \text{with} \quad \tau = (\mu + \mu_t) \cdot |\nabla U \cdot \vec{n}|, \tag{2.44}$$

Equations (2.44) differ in flexibility compared to those of Eq. (2.34), as they directly determine τ on the wall. The researchers propose integrating a novel wall function into the (foam-ext) source code, substituting Eq. (2.38) with a relation grounded in the analogy between momentum and heat transfer.

$$\alpha_t = \frac{\mu_t \cdot \eta \cdot A}{Pr_t} \tag{2.45}$$

The analogy factor η is determined using Eq. (2.43), with A representing a dimensionless constant. In the present paper, A is set to 2, although this can be revised in further investigations. Equations (2.43) and (2.45) have been integrated into the foam-ext source code to alter the wall function known as *alphatRoughWallFunction*. For scenarios where $K_s^+ > 5$, the relationship is described by Eq. (2.38).

This thermal wall function was validated by Lima da Silva et al. (1) for an isothermal rough cylinder with pyramidal roughness. Stefanini et al. (2) and others (10) applied integral boundary layer calculations to the same Achenbach case (28) and modified the St_k Owen-Thomson correlation (29) of Eq. (2.41) to include the roughness of the pyramidal shape because it is more accurate for icing simulation.

(g) Estimation of Sand-Grain Heigth k_s

Ruff (30) defined a correlation to find the sand-grain roughness height depending on LWC, T_∞ and u_∞ based on a constant $(k_s/c0) = 0.00117$ from the experiments.

$$\begin{aligned}
\left[\frac{k_s}{c_0}\right]_{u_\infty} &= 0.4286 + 0.0044139 \cdot u_\infty \\
\left[\frac{k_s}{c_0}\right]_{\mathrm{LWC}} &= 0.5714 + 0.2457 \cdot \mathrm{LWC} + 1.2571 \cdot \mathrm{LWC}^2 \\
\left[\frac{k_s}{c_0}\right]_{T_\infty} &= 46.8384 \cdot \frac{T_\infty}{1000} - 11.2037 \\
k_s &= \left[\frac{k_s}{c_0}\right]_{u_\infty} \cdot \left[\frac{k_s}{c_0}\right]_{\mathrm{LWC}} \cdot \left[\frac{k_s}{c_0}\right]_{T_\infty} \cdot \frac{k_s}{c_0} \cdot c
\end{aligned} \tag{2.46}$$

3. Methodology

(a) Ice Accretion Tool Description

The foam-ext-5.0 numerical simulation library is a continuation of OpenFoam ext 1.6, a fork of the original FOAM code (31) developed by Jasak and Weller at Imperial College in the 1990s (32) and (33). Later, the FOAM code was forked and renamed OpenFoam, which is a recognized solution on the market. The foam-ext code is an old fork of OpenFoam, which was first called OpenFoam ext.

The authors are developing a new tool named iceAccretionFoam, which incorporates standard foam-ext features, such as driftEulerFoam and rhoPimpleFoam solvers, along with some specifically designed extensions, solvers, and functions to perform ice growth and shape simulation, including the IBM and the FAM, for which foam-ext is a pioneer.

(b) Foam-ext Libraries for Icing Simulation

Numerical modeling in ice accretion simulations must account for the significant changes in flow domain geometry caused by the ice accretion on solid walls. The ice changes the shape of the body, and the external flow is affected. To address this, IBM (11) is used, allowing the background mesh to remain unchanged while creating a new surface interpolated within the current mesh points. In addition, the runback water flow is modeled with the support of FAM on the surface of the body, driven by shear forces, pressure gradients, and the momentum of the impinging droplets. The water film height is changed by impinging droplets flux, freezing, and evaporation. The rate of liquid water film height is directly related to the ice growth rate in the presence of freezing phenomena.

(i) Finite Area Method

The FAM, as implemented by Jasak (34), is used to model the movement of liquid water on the surface of the body. Its discretization has the following assumptions:

- The FAM discretizes equations on a curved surface in 3D.
- The surface is discretized using polygonal faces. Discretization takes into account surface curvature. A certain level of smoothness is assumed in the calculation of curvature terms.
- The surface motion is allowed: It is decomposed into normal and tangential motions.
- The nomenclature for a surface element P and its neighbor N.

For the velocity at point P, it can be represented by Eq. (3.1) and Figure 2:

$$\begin{aligned} \overline{\mathbf{v}}_e &= (\mathbf{T}_e)^T \cdot [e_x \mathbf{T}_P \cdot \overline{\mathbf{v}}_P + (1 - e_x)\, \mathbf{T}_N \cdot \overline{\mathbf{v}}_N] \\ e_x &= \frac{\overline{eN}}{\overline{PeN}} \end{aligned} \tag{3.1}$$

(ii) Immersed Boundary Method

The IBM, pioneered by Charles Peskin in 1972 (35), represents a significant advancement in the simulation of fluid flow around complex structures. This method, which focuses particularly on liquid-solid immersed boundaries (IBs), has been adapted for various applications. IBM simplifies meshing for intricate geometries, minimizes computation times, and addresses simulations that are challenging with traditional methods. Further insights into other IB categories are available in (36) and (37).

According to Ketteman (38), Jasak introduced an innovative IBS, a more stable variation of the traditional IBM, in (39). This method aims to treat the immersed geometry in the background mesh in a way similar to a body-fitted mesh, maintaining the original topology of both the background and the surface mesh, unlike the traditional cut-cell approach. Figure 3 visually describes the implementation of IBS

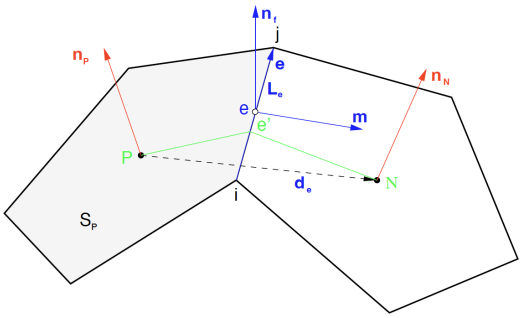

Figure 2: Face-edge interpolation in an edge-based local coordinate system after Jasak (34)

by segmenting three cells. These segmented cells, consisting of live and dead parts, undergo adjustments in their discretization matrix without altering their topology. Modifications pertain to cell center, area, and volume based on the live part. This updated matrix introduces the boundary conditions of the immersed geometry into the background mesh through the formed IB-surface.

As Jasak (39) mentioned when implementing changes in IBM, this new approach to IBS offers several benefits. First, the IB patch is integrated into the mesh using a distance function, allowing cells intersecting the IB to remain active and have their volumes and face areas precisely adjusted. Second, the quality or resolution of the IB STL patch is not critical, as only the closest-distance data is used. Third, the original mesh connectivity is retained after cutting, and the cut cell re-utilizes the discretization matrix slot of the original cell. Lastly, new faces are formed at one per cut cell and included in the immersed patch, with the IB patch face cell addressing identifying the cut cells. This configuration enables the use of standard finite-volume method (FVM) discretization without alterations or polynomial fitting, preserving the topological connectivity and sparseness pattern of the background mesh.

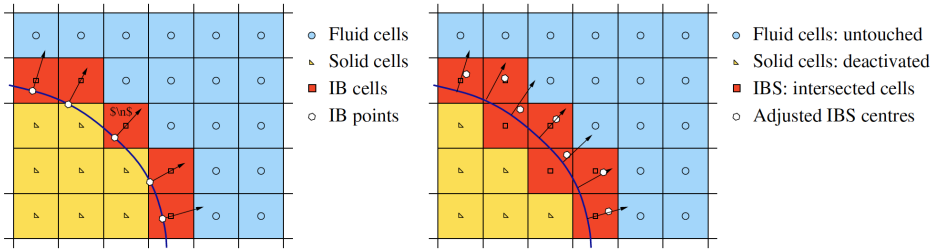

Figure 3: Traditional IBM and New Implementation of IBS after Jasak (39)

Therefore, the IBS is used to change the shape of the airfoil due to ice growth. After a threshold, a new surface STL is created, and the procedure is restarted. An alternative to the IBS method would be to grow the ice, remake the surface, and re-mesh the body, which is an expensive approach in terms of time and resources. Another way would be to deform the mesh cells, which would not work well with glaze ice horns because of the high distortion required.

(c) Code Implementation

The main PIMPLE loop, with an inner loop for pressure p and an outer loop for velocity U and enthalpy h, is followed by the solution of the water film equations for momentum, mass, and energy conservation.

Before closing the loop, the code checks whether it is the appropriate time to grow the ice. The flow solution interval and δ_{ice} time are defined in a dictionary file as input. Before the film equations are solved, there is a function that transfers fields from the IB, such as impingement, shear, momentum of the droplets, and pressure gradient, to the patch where the film is solved. After the solution of height, velocity, and temperature, there is a transfer from the patch where the film is solved to the IB, such as the freezing fraction and the rate of film height as in Eq. (2.27), where the ice grows and the surface is deformed. In addition to the transfer between finite-volume patches, one containing the IB and another where the film resides, there is a transfer between the finite-volume and the finite-area realms, and vice versa, at the patch where the film equations are solved.

A major change in the code is necessary to solve the film on the IB patch. This work is beyond the scope of this paper since developers must code the change, and this paper deals only with the implementation of an icing model with code work related to physical phenomena. Despite the desire of film in IB, the approach of solving the film in another patch is accurate enough because it guarantees that all the boundary conditions are respected and the results are correctly passed. Another possible approach would be to re-mesh after ice growth and solve the film in the new mesh patch. However, this approach is cumbersome and requires more computational effort.

In this paper, the authors implemented two types of functions to transfer the fields from the IB to the film patch. The same function is used to perform the reverse transfer after a mapping in the first variable transfer. The first is the alignment of the normals between the source and target cells, and the second is the alignment of the vector that links the centers of source and target cells with the normal of the source cell. Other mappings, which are native to the IB and finite-volume, can be used and will be tried in the future to improve the results.

The shear of the external flow is evaluated using the effective viscosity μ_{Eff}, determined through the rough turbulent wall functions of the authors. For the film energy equation, the heat transfer coefficient is acquired based on Eqs. (2.22) and (2.23). The effective thermal diffusivity α_{Eff} is derived using the turbulent boundary layer model by Lima da Silva et al. (1), as incorporated in this study.

The logical structure of the solver, detailing the sequence of operations - including parameter initialization, the PIMPLE loop to solve flow properties, updates to the immersed boundary field, and the ice growth routines - is illustrated in the flow chart in Figure 4.

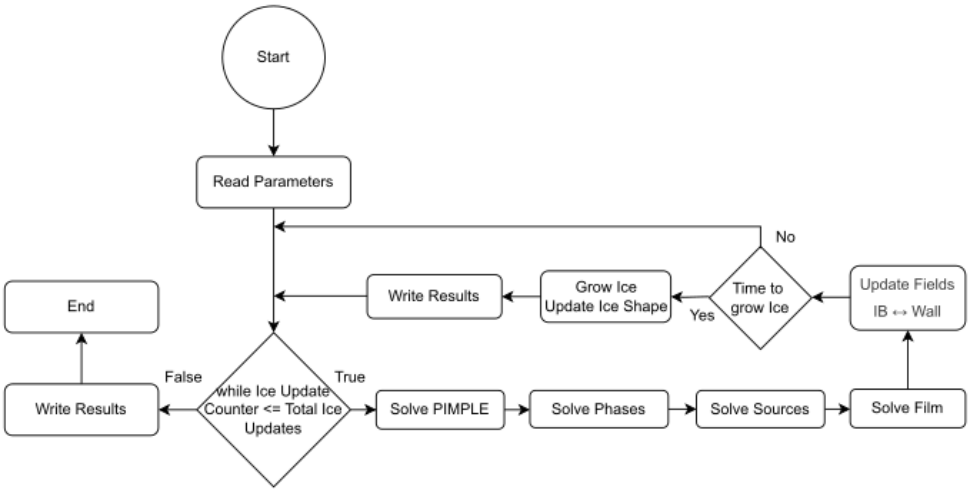

Figure 4: Main IceAccretionFoam code algorithm

(d) Solver Setup and Mesh

The mesh used in this study is composed of O-Type, structured, and hexahedral elements, notably excluding any prism layers. The coarse mesh consists of approximately 7,000 elements. There is no prism layer since this mesh was adopted from previous work (15; 16) to allow comparison and proper testing. However, a finer mesh with a prism layer is important to provide accurate shear and heat transfer results with a controlled y^+ for wall function with roughness elements, accurate finite-area mesh, and proper ice growth using an IB. This mesh has no intent to validate viscous effects, but only macro-behavior of the model. Mesh independence analysis was not performed because the primary objective of this paper is to verify the implementation of the model rather than to achieve a final simulation with comprehensive validation. The mean value of y^+ was approximately 70, with a maximum below 160 near the leading edge, which are values appropriate for the application of wall functions. These values are influenced by the IB interpolation and the refinement of the background mesh since the frontier can be at partial cells. Therefore, they have a fluctuating characteristic. Future studies will focus on background mesh refinement and ice growth using IBM.

Pressure p is the zero-gradient freestream type along all external boundaries, while velocity U is specified as the freestream type with a fixed value. The velocity U_{phase} at the boundaries is equal to U, and there is a zero gradient for the incoming particles and a fixed zero value for the outgoing particles at the faces. The setup of α is similar to U_{phase} for the surface and is given by LWC in the freestream. Both enthalpy h and temperature T have fixed values on the wall to allow the gradient computation to calculate the heat transfer coefficient. However, the temperature of the water film is not passed to the airfoil wall or to the IB patches. The current code does not allow for change because it is a fixed value type of boundary condition and requires the implementation of customized code. However, the error is expected to be small since the surface temperature adopted is close to the film temperature.

The flow is solved in 0.1 s, with Δt_{ice} being 30 s. However, the initial ice accretion begins at 0.2 s to guarantee the finalization of the temperature transient, considering that temperature responds more slowly than pressure.

For the rime and glaze cases simulated in the present paper, the turbulence model k-ϵ, the Second-Order TVD scheme, the AMG solver for p, and the LEWICE ice density correlation are employed. These were the best parameters found in previous work (15; 16) on rime ice shape simulation.

4. Results and Discussion

(a) Test Cases

Shin and Bond (40) tested cases of accumulation of ice on a NACA0012 airfoil with a chord length of 0.53 m at a static free-stream temperature (T_∞) of 247.04 K for rime ice and 270.93 K for glaze ice, with a median volumetric diameter (MVD) of 20 μm, liquid water content (LWC) of 1.0 g/m^3, and free-stream velocity (U_∞) of 67 m/s, all set at a 4° angle of attack. They evaluated the shape of the ice accretion over a 360-second interval for this particular scenario. The authors of the present paper assumed a test section at a pressure altitude of 609.4 m (2000 feet) as this detail was not provided by Shin and Bond (40). The roughness height k_s for the rime ice is estimated to be 0.000342, while for the glaze ice it is 0.001385, as per Eq. (2.46).

For this paper, the Wright droplet distribution (41) is adopted, as it was previously used to validate LEWICE 3.0 software, according to the description in Table 1.

(b) Numerical Results

The numerical results obtained for the rime and glaze cases are presented. The two-phase flow is solved in the IB patch, and the liquid-water film is solved on the original airfoil patch. These two patches need to communicate in both ways because the film receives data from the two-phase flow and sends the results to the IB to deform the surface and represent the ice growth.

The first interpolation scheme is the alignment of source and target cell normals. The rime case, in Fig. 5, shows a satisfactory deviation between the predictions and the experimental data. This confirms Eq. (2.27)

Table 1: Distribution of Wright (41) with MVD = 21 μm.

% LWC	**D(I)** μm
0.1390	8.6
0.0958	12.5
0.0997	15.5
0.1220	18.5
0.1208	21.5
0.1115	24.5
0.0917	27.5
0.0946	31.6
0.0899	48.2
0.0350	95.9

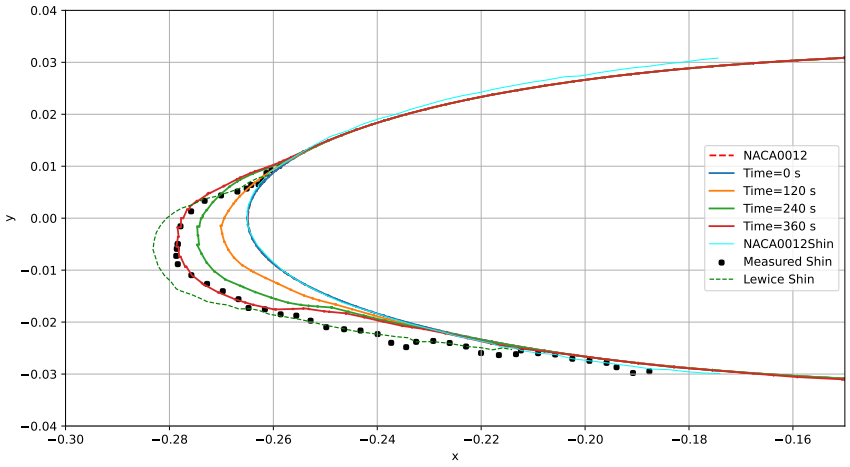

Figure 5: Rime ice case. Transfer function with alignment of cell source and target normals

is correct and that the freezing fraction works when the temperature of the water on the surface is well below the freezing temperature of 273.15 K. The results obtained are comparable to those of previous work that had a simple accretion without a film model (15). The glaze ice shape for the normal transfer type is shown in Fig. 6. It presents a high discrepancy in terms of mass of ice and does not have the horn; however, it indicates that the film is liquid and the freezing fraction is working. The smaller and more spread-out horn-type formation is mainly due to the lack of a laminar-turbulent transition effect, which marks a point of freezing to locally increase the value of the heat transfer coefficient.

The smaller mass of ice compared to the experimental one may be due to an overestimated heat transfer coefficient and, consequently, an overestimated water evaporation. This study considers the heat transfer coefficient to be fully rough and turbulent throughout, likely contributing to elevated evaporation rates. In reality, the areas close to the stagnation point and slightly downstream are laminar, resulting in reduced mass and heat transfer. Furthermore, the laminar segment is not intensified by the presence of roughness. Hence, two aspects are not depicted here in this paper: the laminar regime and a region without heat transfer enhancement because of roughness. Therefore, the lower mass of the ice and the high evaporation are expected effects. The current code is not designed to validate evaporation rates, as it uses a fully turbulent model. Future research will incorporate a laminar-turbulent transition induced by surface roughness, so the mass transfer coefficient will be better represented.

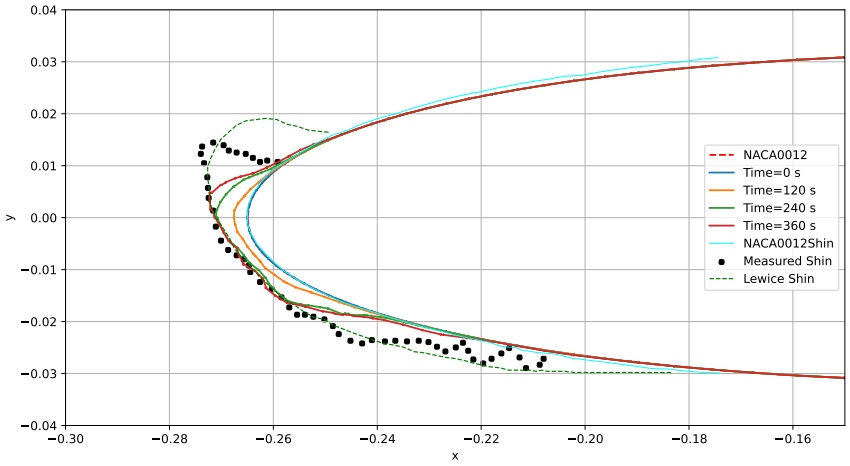

Figure 6: Glaze ice case. Transfer function with alignment of cell source and target normals

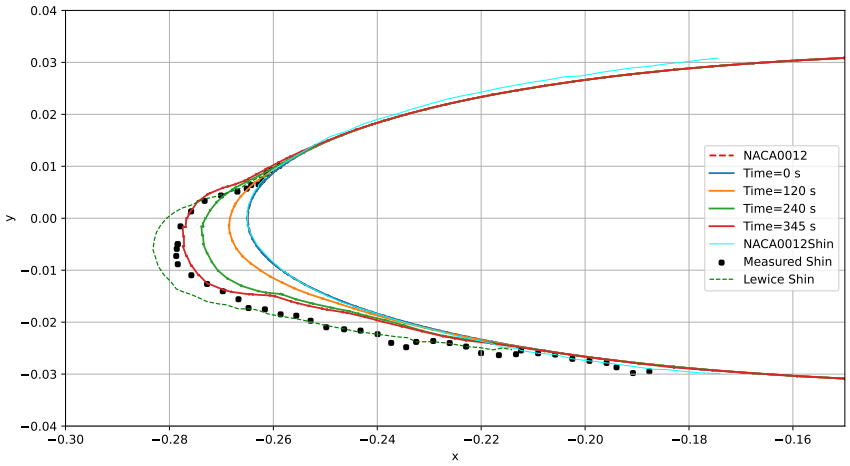

Figure 7: Rime ice case. Transfer function with source normal and cell centers vectors

The second scheme of field transfer is the alignment between the normal source cell and the vector connecting the center of the source and target cells. However, unlike the alignment of both normals, this transfer is done only in one way and is repeated in the reverse way, like a mapping. The reason is that the source normal vector, which defines the orientation of the source cell surface, is specific to the direction of transfer. When the mapping is reversed, the target cell becomes the source, and its normal vector may have a different orientation due to the change in perspective. This directional dependency means that the normal alignment differs between the forward and reverse transfers. It appears from Figs. 7 and 8 that the results had some kind of smoothing, but they are very close to those in the normal transfer type.

Both rime results, Figs 5 and 7 are acceptable in terms of ice simulation; it is noted that the LEWICE simulation performed by Shin and Bond (40), has a larger deviation, as shown in the same plots. Regarding glaze ice, there is an indication of a kink, maybe an incipient horn, in both Figs. 6 and 8. It is clear that the lower part of the ice shape was affected by the high evaporation and the lack of mass of the water film.

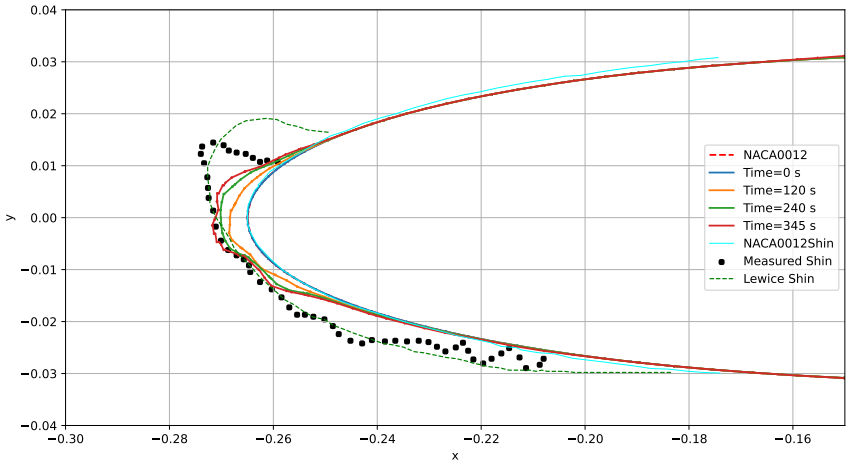

Figure 8: Glaze ice case. Transfer function with source normal and cell centers vectors

However, the film model and the implemented IB proved to be appropriate. Another important fact is that the ice problem is affected by the local values of the heat transfer coefficient but also the average. When laminar, transition, and turbulent regions are absent, there is no transition step from laminar to turbulent, resulting in a higher average heat transfer coefficient, which is further intensified by roughness.

The current model for predicting the glaze ice shape is not considered a definitive solution because of the absence of a laminar-turbulent transition and a comprehensive representation of water surface hydrodynamics. The runback flow is modeled as a continuous film, omitting alternative regimes such as rivulets or beads. Consequently, the predicted glaze ice shape is unlikely to align with experimental findings. However, the code is the pioneer in applying finite-area, Lima da Silva (1) validated rough wall functions, IB and a full URANS for the main flow.

5. Conclusion

The work developed and implemented a glaze and rime ice accretion simulation based on foam-ext 5.0 numerical libraries: the new iceAccretionFoam solver. It is more complete than previous work (15; 16) because it implements the effects necessary for the simulation of glaze ice. Rime ice is also implemented in the new approach of modeling the water film by finite area. It is an important step toward the icing tool within a full 3D CFD code.

The rime ice shapes obtained are closer to the experimental data than the literature results with a classical ice code LEWICE from NASA, USA. In terms of deviation from experimental data, the results are also acceptable for engineering applications. It is important to note that the code does not have a special version for rime; thus, rime and glaze are calculated in the same code and algorithm.

However, simulation of glaze ice shapes, where there is a liquid film of water on the surface because the free-stream temperature is near 273.15 K, showed deviations in ice mass and horn size. The results showed an incipient horn in the correct location and demonstrated that the water-film model worked as expected. The liquid water exists and was driven by external flow momentum sources at the immersed boundary frontier. In addition, the energy conservation of the film worked well, as did the freezing fraction.

In this context, the findings indicated that the implementation of unsteady compressible flow with the energy equation, the mathematical model of a finite area water film, the immersed boundary deformation, as well as the rough wall function for momentum and thermal, were accurately implemented and yielded satisfactory results. It is crucial to note that these implementations are not present in the researched literature, illustrating the innovative methodology employed by the current authors.

The absence of a laminar-turbulent transition model led to increased water evaporation and deviations in the horn's dimensions and shape, despite the location being consistent with experimental data. Laminar heat transfer is lower than turbulent heat transfer and remains unaffected by surface roughness. Ultimately, the shift from laminar to turbulent flow is important for the water freezing process because it enhances the heat transfer coefficient, leading to water freezing as demonstrated by Stefanini et al. (3; 4).

Another important fact is that the rime ice is less affected by the overprediction of evaporated mass, since the freestream temperature is 247.04 K, i.e., far from freezing. This is the main reason, because the deviation is more evident in the glaze than in the rime ice shape.

The present model currently has capabilities that are not implemented in this paper, but will be extended in the future to simulate additional effects required for comprehensive ice simulations, such as:

- Laminar-Turbulent transition modeling, because it increases the heat transfer coefficient at the onset position where the ice horn is approximately located, of which Stefanini et al. emphasized the importance (4) and (2).
- Hydrodynamic regimes of beads, films, and rivulets for the liquid-water runback flow.
- The capability of handling super-large droplets (SLD) with diameters greater than 40 μ m with breaking and splashing effects (42).

In summary, the current code is designed to simulate both rime and glaze results within a single framework. It employs novel methods such as finite-area techniques for runback flow, specialized turbulent wall functions for rough ice surfaces using a suitable momentum to thermal diffusion analogy, an immersed boundary method for ice shapes, including complex ones like glaze ice, and a compressible URANS solution for external flow with a multistep approach. The rime result aligns well with expectations, whereas the glaze represents the initial phase towards full implementation.

References

1 Lima da Silva GA, Arima MN, Branco NN, Pimenta MM. 2011 Proposed Wall Function Models for Heat Transfer around a Cylinder with Rough Surface in Cross Flow. In *SAE 2011 International Conference on Aircraft and Engine Icing and Ground Deicing* number SAE 2011-38-0023 Chicago, IL, USA. (10.4271/2011-38-0023)

2 Stefanini LM, Silvares OM, Lima da Silva GA, Zerbini EGJ. 2010 Heat Transfer on Iced Cylinders. In *AIAA Atmospheric and Space Environments Conference* number AIAA 2010-7672. American Institute of Aeronautics and Astronautics (AIAA). (10.2514/6.2010-7672)

3 Stefanini LM, Silvares OM, Lima da Silva GA, Zerbini EGJ. 2007 Convective Heat Transfer Effects in Airfoil Icing. In *Proceedings of COBEM* Brasilia, Brazil.

4 Stefanini LM. 2009 *Efeitos da camada limite térmica na formação de gelo em aerofólios de uso aeronáutico*. PhD thesis Escola Politécnica da Universidade de São Paulo São Paulo, Brazil.

5 Bidwell CS, Potapczuk MG. 1993 Users Manual for the NASA Lewis Three-Dimensional Ice Accretion Code (LEWICE 3D). Technical Report NASA-TM-105974 NASA Cleveland.

6 Beaugendre H, Morency F, Habashi WG. 2003 FENSAP-ICE's Three-Dimensional In-Flight Ice Accretion Module: ICE3D. *Journal of Aircraft* **40**, 239–247. (10.2514/2.3113)

7 Beld EJ. 2013 Droplet Impingement and Film Layer Modeling as a Basis for Aircraft Icing Simulations in OpenFOAM. Master's thesis University of Twente.

8 Li S, Paoli R. 2019 Modeling of Ice Accretion over Aircraft Wings Using a Compressible OpenFOAM Solver. *International Journal of Aerospace Engineering* **2019**. Article ID 4864927 (10.1155/2019/4864927)

9 Tukovic Z, Jasak H. 2008 Simulation of Free-Rising Bubble with Soluble Surfactant Using Moving Mesh Finite Volume/Area Method. In *6th International Conference on CFD in Oil & Gas, Metallurgical and Process Industries* number CFD08-09 pp. 1–11 SINTEF/NTNU, Trondheim, Norway.

10 Lima da Silva GA, de Barros DR, Pio DM, Rafael CF, Stefanini LM, Pimenta MdM. 2023 Numerical Simulation of Convective Heat Transfer for In-Flight Icing. In Habashi WG, editor, *Handbook of Numerical Simulation of In-Flight Icing* , . Cham: Springer Nature. (10.1007/978-3-030-64725-4$_5$ − 2)

11 Jasak H, Rigler D, Tuković Z. 2014 Design and Implementation of Immersed Boundary Method with Discrete Forcing Approach for Boundary Conditions. In *11th World Congress on Computational Mechanics (WCCM XI)* Barcelona, Spain.
12 Schiller L, Naumann A. 1933 Die grundlagen der gleichungsaufstellung bei der schwebstoffbewegung. *Zeitschrift des Vereins Deutscher Ingenieure* **77**, 318–320.
13 Spalding DB. 1963 *Convective Mass Transfer, an Introduction*. New York: McGraw-Hill.
14 Kays WM, Crawford ME. 1993 *Convective Heat and Mass Transfer*. New York: McGraw-Hill 3rd edition.
15 Teixeira Da Silva JR, Lopes MEC, Preguiça APR, Rafael CF, Souza Villela PC, Lima da Silva GA, Jasak H. 2024 Initial Development of a CFD Icing Tool. In *Proceedings of the International Council of Aeronautical Sciences Conference* Florence, Italy. Paper ICAS 2024-1112.
16 Teixeira Da Silva JR, Rafael CF, Souza Villela PC, Lima da Silva GA, Jasak H. 2025 Introducing the iceAccretionFoam Solver: Impingement and Rime Ice. *Philosophical Transactions of the Royal Society A: Mathematical, Physical and Engineering Sciences* **XX**, XX–XX. Special Issue: Heat and Mass Transfer in Frost and Ice.
17 Wright WB. 1995 Update to the NASA Lewis Ice Accretion Code LEWICE. Contractor Report NASA-CR-198355 NYMA, Inc.
18 Crank J. 1984 *Free and Moving Boundary Problems*. Oxford Science Publications. Oxford: Clarendon Press. Professor Emeritus, Brunel University.
19 Raw MJ, Schneider GE. 1985 A New Implicit Solution Procedure for Multidimensional Finite-Difference Modeling of the Stefan Problem. *Numerical Heat Transfer* **8**, 559–571. (10.1080/01495728508961872)
20 Tapia XP. 2009 Modelling of Wind Flow over Complex Terrain Using OpenFOAM. Master's thesis University of Gävle.
21 Pimenta MM. 1975 *The Turbulent Boundary Layer: An Experimental Study of the Transport of Momentum and Heat with the Effects of Roughness*. PhD thesis Stanford University Stanford, CA.
22 Moffat RJ, Kays WM. 1984 A Review of Turbulent-Boundary-Layer Heat Transfer Research at Stanford, 1958–1983. In Hartnett JP, Thomas F. Irvine J, editors, *Advances in Heat Transfer* pp. 241–365. Elsevier. (10.1016/S0065-2717(08)70206-5)
23 Wright WB. 1995 *User Manual for the Improved NASA Lewis Ice Accretion Code LEWICE 1.6*. Cleveland: National Aeronautics and Space Administration. 95 p. (Contractor Report, 198355).
24 Guffond D, Brunet L. 1988 *Validation du Programme Bidimensionnel de Capitation*. Châtillon Cedex, France: Office National d'Études et de Recherches Aérospatiales. Rapport Technique RP 20/5146 SY.
25 Makkonen L. 1985 Heat Transfer and Icing of a Rough Cylinder. *Cold Regions Science and Technology* **10**, 105–116. (10.1016/0165-232X(85)90022-9)
26 Yaglom AM, Kader BA. 1974 Heat and Mass Transfer between a Rough Wall and Turbulent Fluid Flow at High Reynolds and Peclet Numbers. *Journal of Fluid Mechanics* **62**, 601–623. (10.1017/S0022112074000838)
27 Cebeci T. 2004 *Analysis of Turbulent Flows*. Amsterdam: Elsevier 2nd edition.
28 Achenbach E. 1977 The Effect of Surface Roughness on the Heat Transfer from a Circular Cylinder to the Cross Flow of Air. *International Journal of Heat and Mass Transfer* **20**, 359–369. (10.1016/0017-9310(77)90157-0)
29 Owen PR, Thomson WR. 1963 Heat Transfer Across Rough Surfaces. *Journal of Fluid Mechanics* **15**, 321–334. (10.1017/S0022112063000320)
30 Ruff GA, Berkowitz BM. 1990 Users Manual for the NASA Lewis Ice Accretion Prediction Code (LEWICE). Contractor Report 185129 National Aeronautics and Space Administration Cleveland.
31 Weller HG, Tabor G, Jasak H, Fureby C. 1998 A Tensorial Approach to Computational Continuum Mechanics Using Object-Oriented Techniques. *Computers in Physics* **12**, 620–631. (10.1063/1.168744)
32 Jasak H, Jemcov A, Tuković Z. 2007 OpenFOAM: A C++ Library for Complex Physics Simulations. In *International Workshop on Coupled Methods in Numerical Dynamics* pp. 1–19 IUC, Dubrovnik, Croatia.
33 Jasak H. 2009 OpenFOAM: Open Source CFD in Research and Industry. *International Journal of Naval Architecture and Ocean Engineering* **1**, 89–94. (10.2478/ijnaoe-2013-0011)
34 Jasak H. 2010 Current Development Work in OpenFOAM. In *Dutch OpenFOAM Day* TU Delft, Netherlands.

35 Peskin CS. 1972 Flow Patterns Around Heart Valves: A Numerical Method. *Journal of Computational Physics* **10**, 252–271. (10.1016/0021-9991(72)90065-4)

36 Scardovelli R, Zaleski S. 1999 Direct Numerical Simulation of Free-Surface and Interfacial Flow. *Annual Review of Fluid Mechanics* **31**, 567–603. (10.1146/annurev.fluid.31.1.567)

37 Anderson DM, McFadden GB, Wheeler AA. 1998 Diffuse-Interface Methods in Fluid Mechanics. *Annual Review of Fluid Mechanics* **30**, 139–165. (10.1146/annurev.fluid.30.1.139)

38 Kettemann J, Bonten C. 2020 Application of the Immersed Boundary Surface Method in OpenFOAM. In *Fracture and Damage Mechanics: Theory, Simulation and Experiment*. AIP Publishing. (10.1063/5.0028625)

39 Jasak H. 2018 Immersed Boundary Surface Method in Foam-Extend. In *The 13th OpenFOAM Workshop (OFW13)* pp. 55–59.

40 Shin J, Bond TH. 1992 Experimental and Computational Ice Shapes and Resulting Drag Increase for a NACA 0012 Airfoil. Technical Memorandum 105743 NASA. 5th Symposium on Numerical and Physical Aspects of Aerodynamic Flows, California State University, Long Beach, California.

41 Wright WB. 2005 Validation Results for LEWICE 3.0. NASA Contractor Report NASA/CR-2005-213561 NASA Cleveland, OH, United States. Available at NASA Technical Reports Server (NTRS).

42 Wright W, Potapczuk M, Levinson L. 2008 Comparison of LEWICE and GlennICE in the SLD Regime. In *46th AIAA Aerospace Sciences Meeting and Exhibit* number AIAA 2008-439. American Institute of Aeronautics and Astronautics (AIAA). (10.2514/6.2008-439)